Article

Geostrophic flows control future changes of oceanic eastern boundary upwelling

Check for updates

Zhao Jing [1,2,3], Shengpeng Wang[1,2,3], Lixin Wu [1,2] ✉, Hong Wang [1,2], Shenghui Zhou[2], Bingrong Sun[1,2], Zhaohui Chen [1,2], Xiaohui Ma [1,2], Bolan Gan [1,2] & Haiyuan Yang[1,2]

Equatorward alongshore winds over major eastern boundary upwelling systems (EBUSs) drive intense upwelling via Ekman dynamics, surfacing nutrient-rich deep waters and promoting marine primary production and fisheries. It is generally thought, dating back to Bakun's hypothesis, that greenhouse warming should enhance upwelling in EBUSs by intensifying upwelling-favourable winds; yet this has not been tested. Here, using an ensemble of high-resolution climate simulations with improved EBUS representation, we show that long-term upwelling changes in EBUSs differ substantially, under a high-emission scenario, from those inferred by the wind-based upwelling index. Specifically, weakened or unchanged upwelling can coincide with intensified upwelling-favourable winds. These differences are linked to long-term changes of geostrophic flows that dominate upwelling changes in the Canary and Benguela currents and strongly offset wind-driven changes in the California and Humboldt currents. Our results highlight the controlling role of geostrophic flows in upwelling trends in EBUSs under greenhouse warming, which Bakun's hypothesis overlooked.

The eastern boundary upwelling systems (EBUSs), including the California, Humboldt, Canary and Benguela current systems, are among the most biologically productive ecosystems, covering less than 2% of the ocean surface but contributing 7% to global marine primary production and more than 20% to global fish catches (Fig. 1)[1–3]. The equatorward alongshore winds favoured by the large-scale atmospheric pressure systems transport the surface waters offshore via the Ekman dynamics, causing them to be replaced by nutrient-rich deep waters that are essential to sustain the high-level productivity in the EBUSs[4–6]. How the upwelling in the EBUSs responds to anthropogenic climate changes, therefore, has profound global environmental and socioeconomic impacts and is an enduring scientific issue in biological and climatic sciences[7,8].

Due to the sparsity of existing in situ ocean current measurements, the upwelling in the EBUSs is typically estimated from the wind-based upwelling indices (WUIs) under the premise that the wind-induced Ekman transport is the sole driver of upwelling[4,5,9]. Recognizing the validity of WUIs, Bakun[10] proposed a hypothesis that greenhouse warming should enhance the upwelling in the EBUSs by intensifying the upwelling-favourable winds due to the increased cross-shore atmospheric sea-level pressure gradient. Bakun's hypothesis has stimulated tremendous efforts in investigating the long-term change of upwelling-favourable winds in the EBUSs on the basis of historical observations and climate simulations[7,8,11–16]. The findings generally support Bakun's[10] hypothesis, especially in the high-latitude regions of EBUSs except for the California Current.

Despite the prevailing use of WUIs for assessing the effects of greenhouse warming on the upwelling in the EBUSs, it is arguable that the Ekman theory is an incomplete description of upwelling dynamics in these regions. For example, there is evidence that the cross-shore geostrophic flows associated with the alongshore sea surface height gradient contribute nonnegligibly to the climatological mean upwelling and its long-term changes in some EBUSs, which motivates the refinement of upwelling indices[17–20]. This casts doubts on the long-term changes of upwelling inferred from the WUIs. Furthermore, the WUIs can be used only to estimate the upwelling at

[1]Frontiers Science Center for Deep Ocean Multispheres and Earth System and Key Laboratory of Physical Oceanography, Ocean University of China, Qingdao, China. [2]Laoshan Laboratory, Qingdao, China. [3]These authors contributed equally: Zhao Jing, Shengpeng Wang. ✉e-mail: lxwu@ouc.edu.cn
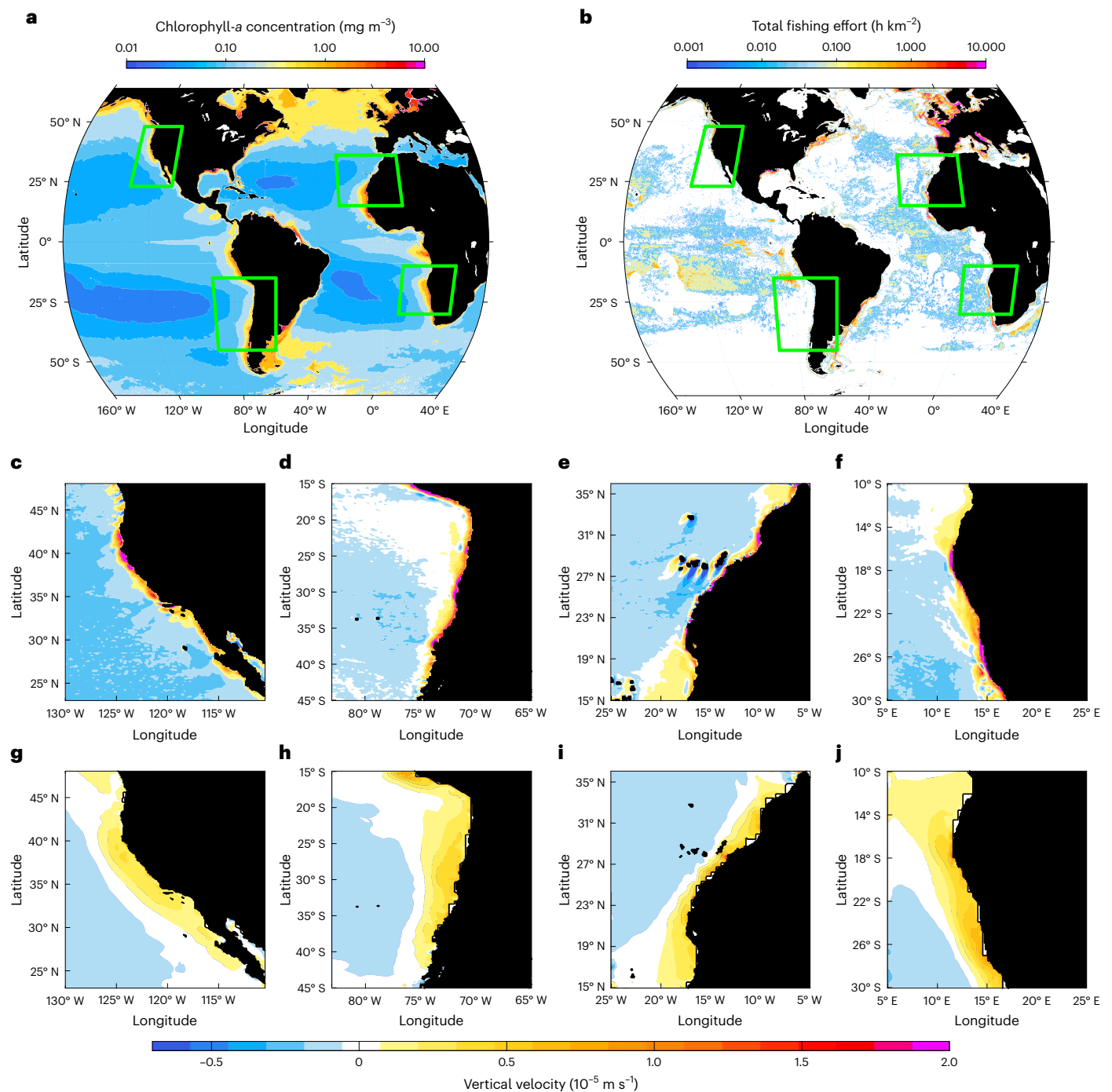
Fig. 1 | Simulated upwelling in the EBUSs in CESM-H and CMIP6 CGCMs.
a,b, Geographic distribution of time-mean ocean chlorophyll-*a* concentration during 2002–2022 (**a**) and fishing efforts during 2012–2021 (**b**). **c**–**f**, The 1920–2005 annual-mean vertical velocity at 50 m in the CalCS (**c**), HCS (**d**), CanCS (**e**) and BCS (**f**) simulated in the CESM-H ensemble mean. **g**–**j**, The 1920–2005 annual-mean vertical velocity at 50 m in the CalCS (**g**), HCS (**h**), CanCS (**i**) and BCS (**j**) simulated in the CMIP6 CGCM ensemble mean. Regions shallower than 50 m in **c**–**j** are masked in black according to the bathymetry of CESM-H.

the base of the surface Ekman layer but provide no information on the vertical structure of upwelling. The latter affects the source depth of upwelled waters, which is closely related to the efficacy of upwelling in fuelling biological productivity[21]. Extension of a two-dimensional Ekman model[22] by incorporating the effects of geostrophic flows demonstrates that the geostrophic flows play an important role not only in regulating the intensity of upwelling but also its vertical structure[17].

Climate simulations make it possible to directly evaluate the response of upwelling in the EBUSs to greenhouse warming on the basis

of the model-simulated vertical water velocity. However, the current generation of coupled global climate models (CGCMs) is generally too coarse to resolve essential dynamics in the EBUSs[7,17,22–30]. In this study, we comprehensively analyse the long-term changes of upwelling in the four major EBUSs (the California Current System (CalCS), Humboldt Current System (HCS), Canary Current System (CanCS) and Benguela Current System (BCS)) under a high carbon-emission scenario, using an ensemble of state-of-the-art high-resolution climate simulations based on a Community Earth System Model (CESM) with an oceanic resolution of 0.1° and atmospheric resolution of 0.25° (CESM-H).
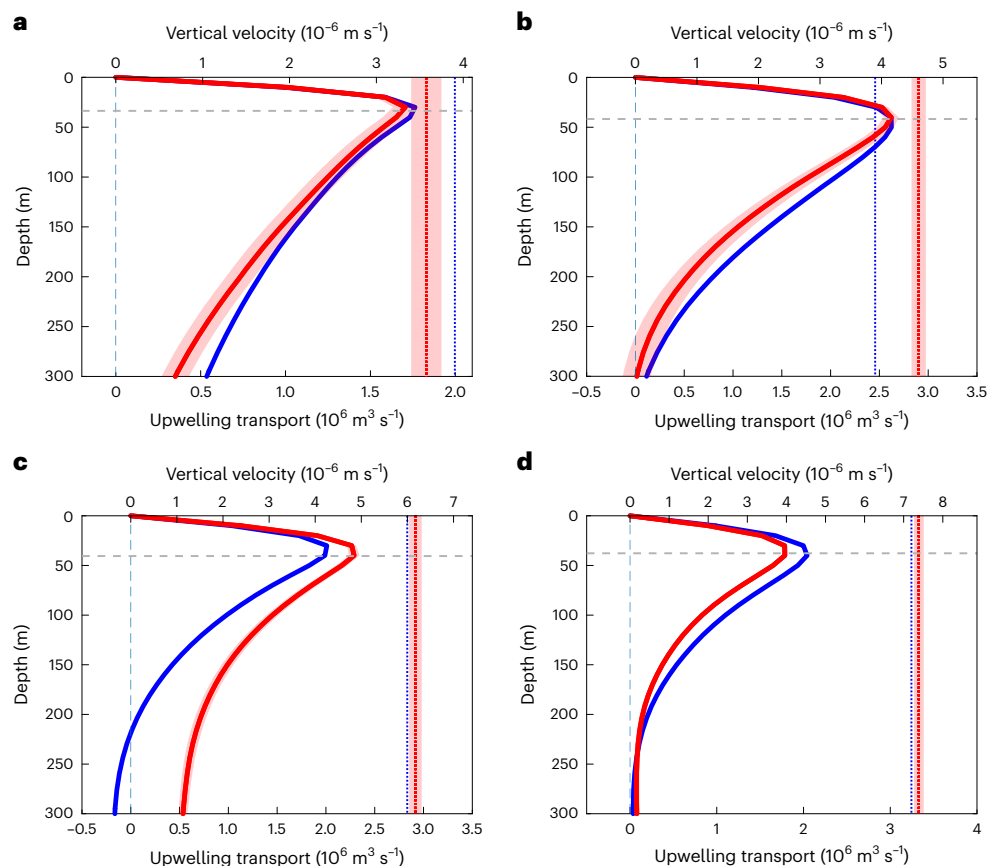
Fig. 2 | Vertical profiles of upwelling transport in the four major EBUSs.
a, CalCS. **b**, HCS. **c**, CanCS. **d**, BCS. The blue and red solid (dotted) lines show the 1920–2005 annual-mean upwelling transport (WUI) and its long-term projection at the end of 21st century for the CESM-H ensemble mean, respectively. The shading denotes the 90% confidence interval for the projected value defined as the long-term change estimated from the linear trend during 2006–2100 added to the mean value during 1920–2005. The horizontal dashed line denotes the 1920–2005 annual-mean surface Ekman layer depth measured as the surface boundary layer depth available in the CESM-H model output. The axes of vertical velocity measure the values of upwelling transport and WUI divided by the integration area. The sample size (the number of time records used to derive the confidence interval) is 95.

Result

Consistent with the existing theoretical arguments and high-resolution regional ocean simulations[24–30], the simulated upwelling in the four EBUSs by CESM-H consists of a rapid coastal component driven by the alongshore wind stress and confined to a narrow band (<50 km) next to the coast and a slower component driven by the wind stress curl and extending further offshore (Fig. 1c–f). By contrast, the simulated upwelling by an ensemble of coarser-resolution CGCMs (Extended Data Table 1) participating in the Coupled Model Intercomparison Project phase 6 (CMIP6)[23] is weaker and more diffusive (Fig. 1g–j), with the prominent coastal upwelling zone being absent. The outperformance of CESM-H over CMIP6 CGCMs in representing the upwelling in the EBUSs can be further inferred from the alleviated warm sea surface temperature (SST) bias in these regions (Extended Data Fig. 1), in view of the strong imprint of upwelling on SST[31,32]. Improved upwelling simulation in CESM-H is attributed primarily to a better resolution of coastal upwelling[17,22] and may also benefit from a more realistic representation of the cross-shore wind stress structure, seafloor topography and oceanic mesoscale eddies[26,29,33–36], which all connect to the high resolution in oceanic or atmospheric model configurations.

Note that even CESM-H is not fine enough to well resolve the coastal upwelling, resulting in an overly wide coastal upwelling zone relative to the reality[17,22,30,34]. On the one hand, a further increase of the oceanic model resolution would probably make the coastal upwelling stronger and narrower until it is fully resolved. On the other hand, the integrated vertical velocity over a sufficiently wide region should be

less sensitive to the model resolution and more faithfully simulated by CESM-H. For this reason, we integrate the vertical velocity within ~200 km from the coast in the individual EBUSs, referred to as the upwelling transport henceforth (Upwelling transport), and compare their long-term changes under greenhouse warming with those inferred from the WUIs. Such integration covers the coastal upwelling and a large fraction of offshore wind stress curl-driven upwelling, both of which are suggested to influence the ecosystem[6]. For the climatological mean upwelling transport in the EBUSs, it peaks around 30–40 m, comparable to the surface Ekman layer depth, and attenuates rapidly further downwards (Fig. 2). This vertical structure of upwelling transport is consistent with the dominant role of winds in driving the upwelling via the Ekman dynamics[24]. Indeed, a particular WUI used in this study (WUI) is comparable to the peaking value of upwelling transport in the vertical (upwelling transport intensity (UTI)) for the individual EBUSs. Despite such qualitative agreement, there are noticeable quantitative differences between the WUI and UTI, especially in the CanCS and BCS, where the WUI overestimates the UTI by about 40% and 60%, respectively. This overestimation is ascribed primarily to the downwelling caused by the convergent geostrophic flows in the CanCS and BCS (Extended Data Fig. 2).

The closeness between the WUI and UTI for the climatological mean state does not extend to their long-term changes under greenhouse warming (Fig. 3a–d). In the CalCS and HCS, the fitted linear trends of WUI during 2006–2100 are -1.6×10^5 m^3 s^{-1} and 4.5×10^5 m^3 s^{-1} per century, respectively. They severely overestimate the trends of UTI
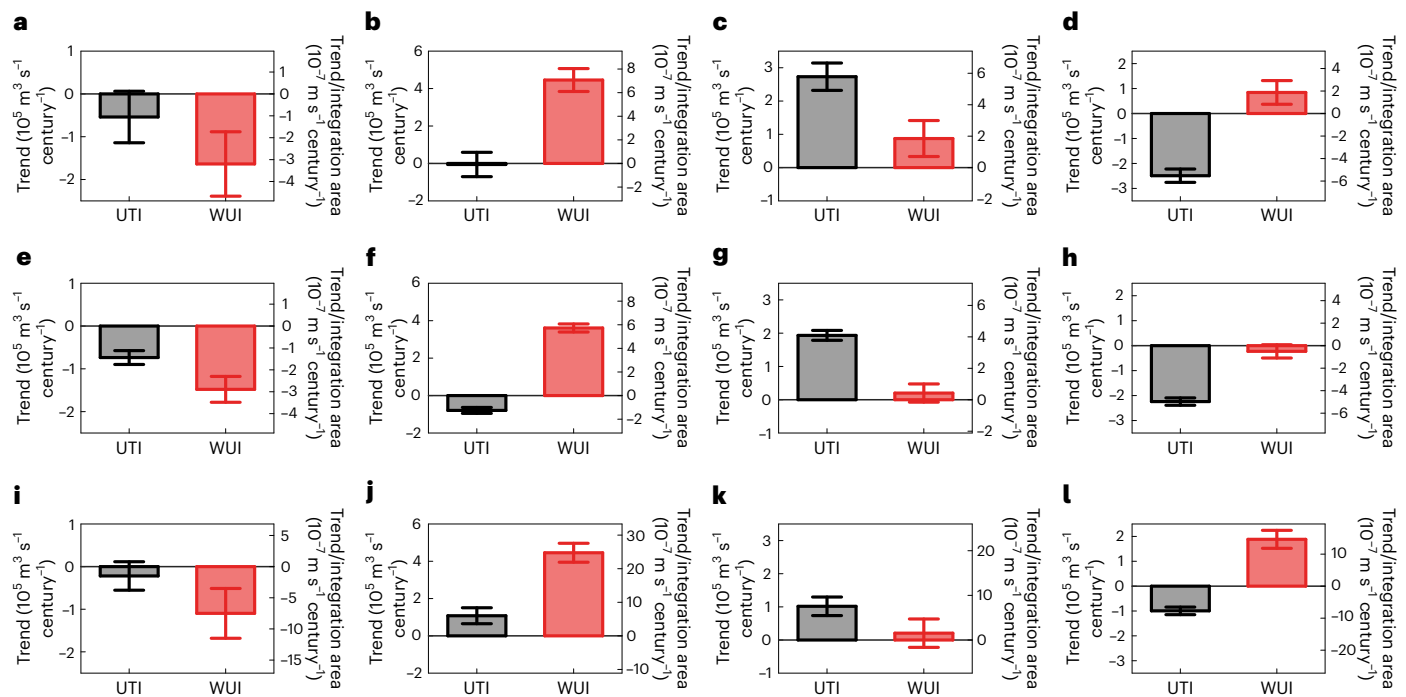
Fig. 3 | Relationship between the long-term changes of annual-mean UTI and WUI in the EBUSs under greenhouse warming. a–l, The slope of the linear trend of annual-mean UTI and WUI (**a–h**) and coastal UTI and WUI (**i–l**) during 2006–2100 for the CESM-H ensemble mean (**a–d,i–l**) and CMIP6 CGCM ensemble mean (**e–h**) in the CalCS (**a,e,i**), HCS (**b,f,j**), CanCS (**c,g,k**) and BCS (**d,h,l**). The error bars denote the 90% confidence interval for the slope. The right axes measure the values of UTI and WUI trends divided by the integration area. The sample size (the number of time records used to derive the confidence interval) is 95.

(-0.5×10^5 m^3 s^{-1} and -0.1×10^5 m^3 s^{-1} per century) that are statistically insignificant at the 90% confidence level. In the CanCS, the UTI has a trend of 2.7×10^5 m^3 s^{-1} per century, about three times the 0.9×10^5 m^3 s^{-1} per century inferred from the WUI. For the BCS, the trend of UTI is negative (-2.5×10^5 m^3 s^{-1} per century) whereas the WUI predicts a positive trend of 0.8×10^5 m^3 s^{-1} per century, suggesting concurrence of weakened upwelling and enhanced upwelling-favourable winds. We remark that the evident decoupling between the trends of WUI and UTI in the EBUSs is not specific to CESM-H but qualitatively reproduced by CMIP6 CGCMs (Fig. 3e–h), providing strong evidence on its robustness. There are, however, quantitative differences between the projected trends in CESM-H and CMIP6 CGCMs, which is due partially to the insufficient resolution of CMIP6 CGCMs in representing the upwelling dynamics.

As suggested by Bakun's hypothesis, the long-term change of upwelling-favourable winds in a warming climate should be more evident in the warm season[10],[11]. To avoid degrading the validity of WUI in representing the response of UTI to greenhouse warming, we repeat the preceding analysis for the warm season only. Despite some quantitative differences from the annual-mean case, the basic conclusion that the long-term change of UTI under greenhouse warming is decoupled from that of WUI still holds in the HCS, CanCS and BCS (Extended Data Fig. 3). In the CalCS, the trends of WUI and UTI in the warm season are qualitatively consistent, but the former is about 40% larger in magnitude than the latter. In addition, given the latitude-dependent long-term change of upwelling-favourable winds[12], we examine the relationship between the trends of WUI and UTI at different latitudes. Their values differ substantially from each other over a large fraction of latitude bands in all the four EBUSs, lending further support to our argument (Extended Data Fig. 4).

Considering the distinctive underlying dynamics and ecological impacts of the rapid coastal upwelling, we recompute the WUI and UTI for the approximately 50-km-wide coastal zone (Fig. 3i–l). The trends of coastal WUI and UTI diverge greatly, with their differences in the

individual EBUSs resembling those calculated for the approximately 200-km-wide upwelling band from the coast. Such resemblance suggests that the decoupling between the long-term changes of WUI and UTI under greenhouse warming is a robust feature that is not sensitive to the width of the upwelling band selected for analysis.

The WUI does not and is not intended to provide any measurement of upwelling transport below the surface Ekman layer. Yet it is found that the long-term change of upwelling transport is more evident in the thermocline than at the surface Ekman layer base in all the EBUSs except the BCS (Fig. 2). This feature is a strong implication that other processes aside from the wind-driven Ekman transport play a crucial role in the response of upwelling to greenhouse warming. Moreover, as the upwelling transport in the thermocline affects the source depth of upwelled waters, its change in a warming climate is likely to have an influence on the efficacy of upwelling in nourishing the ecosystem[21], which cannot be captured by the WUI.

To shed light on the underlying processes accounting for the decoupled responses of WUI and UTI to greenhouse warming, we decompose the upwelling transport into components associated with the horizontal mass-flux divergence caused by geostrophic and ageostrophic flows (referred to as the geostrophic and ageostrophic upwelling transports), respectively (Upwelling transport). This decomposition is made for only one member of the CESM-H ensemble due to the unavailability of sea surface height in the model output of the other two members. Nevertheless, similarity in the trends of upwelling transport among the three members (Extended Data Fig. 5) provides us confidence that the decomposition results derived from any member should be qualitatively representative of the ensemble mean. In all four EBUSs, the climatological mean ageostrophic upwelling transport and its long-term change under greenhouse warming are comparable to those of WUI below the surface Ekman layer (Fig. 4 and Extended Data Fig. 2), suggesting that the ageostrophic upwelling transport is attributed largely to the horizontal mass-flux divergence caused by wind-driven Ekman transport. Although the geostrophic
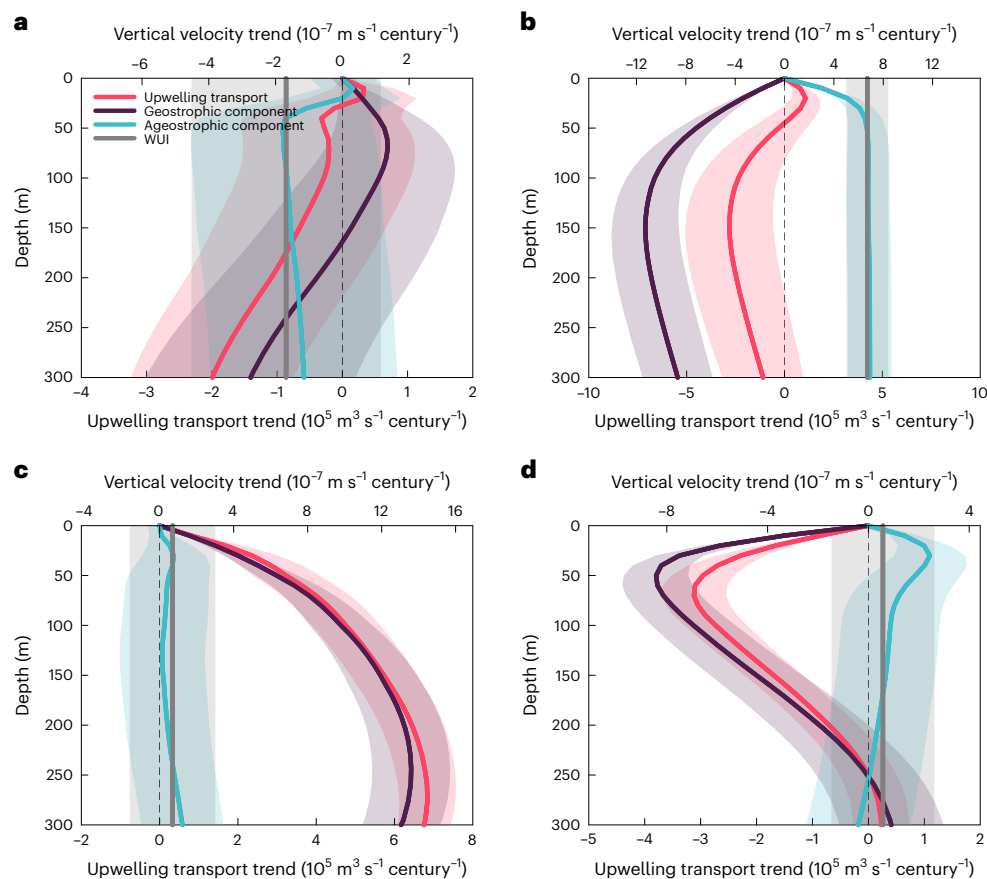
Fig. 4 | Effects of geostrophic flows on the long-term changes of upwelling transport in the EBUSs under greenhouse warming. a–d, The slope of the linear trend of annual-mean upwelling transport (red) during 2006–2100 and its decomposition into components caused by horizontal mass-flux divergence of geostrophic (purple) and ageostrophic (blue) flows for one member of CESM-H in the CalCS (**a**), HCS (**b**), CanCS (**c**) and BCS (**d**). The grey line denotes the slope of the linear trend of WUI. The shading denotes the 90% confidence interval for the slope. The axes of the vertical velocity trend measure the values of the upwelling transport trend divided by the integration area. The sample size (the number of time records used to derive the confidence interval) is 95.

upwelling transport contributes negligibly (CalCS and HCS) or secondarily (CanCS and BCS) to the climatological mean UTI, its contribution to the long-term change of UTI becomes much more important and is primarily responsible for the difference between the trends of WUI and UTI (Fig. 4 and Extended Data Fig. 2). In particular, the trend of geostrophic upwelling transport peaks in the thermocline in the CalCS, HCS and CanCS but not the BCS, explaining the more pronounced long-term changes of upwelling transport in the thermocline than at the surface Ekman layer base in the former three EBUSs.

Discussion

This study reveals the crucial role of geostrophic flows in controlling the response of upwelling to greenhouse warming in the EBUSs, providing new insights overlooked by the existing literature[7,10–14]. It is generally thought that the intensified stratification in a warming climate should cause shoaling of the source of upwelled waters[7,8,14,37]. However, the enhanced geostrophic upwelling transport in the thermocline of CanCS is likely to deepen the source of upwelled waters despite the stronger stratification under greenhouse warming (Fig. 2c and Extended Data Fig. 6). Moreover, the role of geostrophic flows is not uniform among the four EBUSs. It is more prominent in the EBUSs in the Atlantic basin (CanCS and BCS) than in the Pacific basin (CalCS and HCS), in terms of both the climatological mean state and long-term change of upwelling. Previous limited assessment on the effects of geostrophic flows on the long-term change of upwelling happens to be in the Pacific EBUSs[18,20], which underestimates the fundamental contribution of

geostrophic flows to the response of upwelling in the global EBUSs to greenhouse warming.

So far, effects of anthropogenic climate changes on the ecosystems in the EBUSs remain poorly understood. There is an ongoing debate about to what extent the long-term change of biological productivity of EBUS ecosystems is related to that of upwelling in a warming climate[7,8,30]. In addition to the upwelling, the responses of SST, stratification and mesoscale eddy field to greenhouse warming and their interactions with the upwelling are all suggested to play an important role[7,8,21,38]. In particular, the mesoscale eddies, generated primarily through the baroclinic instability of upwelling jet[36,39], transport the nutrient offshore[26] and heat onshore[36], counteracting the effects of upwelling on the coastal SST and nutrient supply. It is thus important to understand the changes of mesoscale eddies and their interactions with the upwelling changes under greenhouse warming. There is some evidence that the mesoscale eddies in CalCS would become stronger under a high carbon-emission scenario due to the enhanced baroclinic instability of upwelling jet caused by intensified upper-ocean stratification[40,41]. However, it remains unclear whether a stronger mesoscale eddy activity in response to greenhouse warming is universal among all the EBUSs and what its implication on the ecosystem is. Simulation of mesoscale eddies is beyond the resolution capacity of most CMIP6 CGCMs but is possible for CESM-H. Coupled with a reliable biogeochemical model, CESM-H can provide us with a better knowledge of the response of EBUS ecosystems to greenhouse warming and its underlying dynamics.

Online content

Any methods, additional references, Nature Portfolio reporting summaries, source data, extended data, supplementary information, acknowledgements, peer review information; details of author contributions and competing interests; and statements of data and code availability are available at https://doi.org/10.1038/s41558-022-01588-y.

References

1. Pauly, D. & Christensen, V. Primary production required to sustain global fisheries. *Nature* **374**, 255–257 (1995).
2. Cochrane, K., De Young, C., Soto, D. & Bahri, T. *Climate Change Implications for Fisheries and Aquaculture* Fisheries and Aquaculture Technical Paper 530 (FAO, 2009).
3. Kroodsma, D. A. et al. Tracking the global footprint of fisheries. *Science* **359**, 904–908 (2018).
4. Bakun, A. *Coastal Upwelling Indices, West Coast of North America, 1946–1971* (NOAA Tech. Rep. NMFS SSRF-671, U.S. Dept. of Commerce, 1973).
5. Bakun, A. *Daily and Weekly Upwelling Indices, West Coast of North America, 1967–1973* (NOAA, 1975).
6. Rykaczewski, R. R. & Checkley, D. M. Jr Influence of ocean winds on the pelagic ecosystem in upwelling regions. *Proc. Natl Acad. Sci. USA* **105**, 1965–1970 (2008).
7. García-Reyes, M. et al. Under pressure: climate change, upwelling, and eastern boundary upwelling ecosystems. *Front. Mar. Sci.* **2**, 109 (2015).
8. Abrahams, A., Schlegel, R. W. & Smit, A. J. Variation and change of upwelling dynamics detected in the world's eastern boundary upwelling systems. *Front. Mar. Sci.* **8**, 626411 (2021).
9. Schwing, F. B., O'Farrell, M., Steger, J. M. & Baltz, K. *Coastal Upwelling Indices West Coast of North America* Technical Report NMFS SWFSC 231 (NOAA, 1996).
10. Bakun, A. Global climate change and intensification of coastal ocean upwelling. *Science* **247**, 198–201 (1990).
11. Sydeman, W. et al. Climate change and wind intensification in coastal upwelling ecosystems. *Science* **345**, 77–80 (2014).
12. Casabella, N., Lorenzo, M. & Taboada, J. Trends of the Galician upwelling in the context of climate change. *J. Sea Res.* **93**, 23–27 (2014).
13. Wang, D., Gouhier, T. C., Menge, B. A. & Ganguly, A. R. Intensification and spatial homogenization of coastal upwelling under climate change. *Nature* **518**, 390–394 (2015).
14. Oyarzún, D. & Brierley, C. M. The future of coastal upwelling in the Humboldt Current from model projections. *Clim. Dyn.* **52**, 599–615 (2019).
15. Rykaczewski, R. R. et al. Poleward displacement of coastal upwelling-favorable winds in the ocean's eastern boundary currents through the 21st century. *Geophys. Res. Lett.* **42**, 6424–6431 (2015).
16. Bonino, G., Di Lorenzo, E., Masina, S. & Iovino, D. Interannual to decadal variability within and across the major eastern boundary upwelling systems. *Sci. Rep.* **9**, 1–14 (2019).
17. Marchesiello, P. & Estrade, P. Upwelling limitation by onshore geostrophic flow. *J. Mar. Res.* **68**, 37–62 (2010).
18. Echevin, V. et al. Sensitivity of the Humboldt Current System to global warming: a downscaling experiment of the IPSL-CM4 model. *Clim. Dyn.* **38.3**, 761–774 (2012).
19. Jacox, M. G., Edwards, C. A., Hazen, E. L. & Bograd, S. J. Coastal upwelling revisited: Ekman, Bakun, and improved upwelling indices for the US West Coast. *J. Geophys. Res. Oceans* **123**, 7332–7350 (2018).
20. Ding, H., Alexander, M. A. & Jacox, M. G. Role of geostrophic currents in future changes of coastal upwelling in the California Current System. *Geophys. Res. Lett.* **48**, e2020GL090768 (2021).
21. Roemmich, D. & McGowan, J. Climatic warming and the decline of zooplankton in the California Current. *Science* **267**, 1324–1326 (1995).
22. Estrade, P., Marchesiello, P., De Verdière, A. C. & Roy, C. Cross-shelf structure of coastal upwelling: a two-dimensional extension of Ekman's theory and a mechanism for inner shelf upwelling shut down. *J. Mar. Res.* **66**, 589–616 (2008).
23. Eyring, V. et al. Overview of the Coupled Model Intercomparison Project Phase 6 (CMIP6) experimental design and organization. *Geosci. Model Dev.* **9**, 1937–1958 (2016).
24. Gill, A. E. & Adrian, E. *Atmosphere–Ocean Dynamics* Vol. 30 (Academic Press, 1982).
25. Enriquez, A. & Friehe, C. Effects of wind stress and wind stress curl variability on coastal upwelling. *J. Phys. Oceanogr.* **25**, 1651–1671 (1995).
26. Gruber, N. et al. Eddy-induced reduction of biological production in eastern boundary upwelling systems. *Nat. Geosci.* **4**, 787–792 (2011).
27. Jacox, M., Moore, A., Edwards, C. & Fiechter, J. Spatially resolved upwelling in the California Current System and its connections to climate variability. *Geophys. Res. Lett.* **41**, 3189–3196 (2014).
28. Nagai, T. et al. Dominant role of eddies and filaments in the offshore transport of carbon and nutrients in the California Current System. *J. Geophys. Res. Oceans* **120**, 5318–5341 (2015).
29. Renault, L., Hall, A. & McWilliams, J. C. Orographic shaping of US West Coast wind profiles during the upwelling season. *Clim. Dyn.* **46**, 273–289 (2016).
30. Renault, L. et al. Partial decoupling of primary productivity from upwelling in the California Current system. *Nat. Geosci.* **9**, 505–508 (2016).
31. Benazzouz, A. et al. An improved coastal upwelling index from sea surface temperature using satellite-based approach—the case of the Canary Current upwelling system. *Cont. Shelf Res.* **81**, 38–54 (2014).
32. Varela, R., Lima, F. P., Seabra, R., Meneghesso, C. & Gómez-Gesteira, M. Coastal warming and wind-driven upwelling: a global analysis. *Sci. Total Environ.* **639**, 1501–1511 (2018).
33. Preller, R. & OBRIEN, J. J. The influence of bottom topography on upwelling off Peru. *J. Phys. Oceanogr.* **10**, 1377–1398 (1980).
34. Capet, X., Marchesiello, P. & McWilliams, J. Upwelling response to coastal wind profiles. *Geophys. Res. Lett.* **31**, L13311 (2004).
35. Lentz, S. J. & Chapman, D. C. The importance of nonlinear cross-shelf momentum flux during wind-driven coastal upwelling. *J. Phys. Oceanogr.* **34**, 2444–2457 (2004).
36. Marchesiello, P., McWilliams, J. C. & Shchepetkin, A. Equilibrium structure and dynamics of the California Current System. *J. Phys. Oceanogr.* **33**, 753–783 (2003).
37. Sousa, M. C. et al. NW Iberian Peninsula coastal upwelling future weakening: competition between wind intensification and surface heating. *Sci. Total Environ.* **703**, 134808 (2020).
38. Bakun, A. et al. Anticipated effects of climate change on coastal upwelling ecosystems. *Curr. Clim. Change Rep.* **1**, 85–93 (2015).
39. Veneziani, M., Edwards, C. A., Doyle, J. D. & Foley, D. A central California coastal ocean modeling study: 1. Forward model and the influence of realistic versus climatological forcing. *J. Geophys. Res. Oceans* **114**, C04015 (2009).
40. Marchesiello, P. & Estrade, P. Eddy activity and mixing in upwelling systems: a comparative study of Northwest Africa and California regions. *Int. J. Earth Sci.* **98**, 299–308 (2009).
41. Quirós, N. C., Jacox, M. G., Buil, M. P. & Bograd, S. J. Future changes in eddy kinetic energy in the California Current System from dynamically downscaled climate projections. *Geophys. Res. Lett.* **49**, e2022GL099042 (2022).

Methods

CESM-H

The CESM-H ensemble, including three members (CESM-H1, CESM-H2 and CESM-H3), is based on CESM version 1.3 (CESM1.3), whose atmospheric component is the Community Atmosphere Model version 5 (CAM5), the oceanic component is the Parallel Ocean Program version 2 (POP2), the sea-ice component is the Community Ice Code version 4 (CICE4) and the land component is the Community Land Model version 4 (CLM4)[42]. The POP2 and CICE4 use the same nominal horizontal resolution of ~0.1°, and the CAM5 and CLM4 use the same nominal horizontal resolution of ~0.25°. The CAM5 and POP2 have 30 and 62 vertical levels, respectively. CESM-H1 consists of a 500-year-long pre-industrial control (PI-CTRL) climate simulation and a historical-and-future transient (HF-TNST) climate simulation from 1850 to 2100, branched from the PI-CTRL at year 250. The HF-TNST uses the historical forcing for 1850–2005 and representative concentration pathway 8.5 forcing for 2006–2100, following the protocol for the CMIP5 experiments[43]. Readers are suggested to refer to ref. [42] for detailed model configurations. CESM-H2 and CESM-H3 are branched from CESM-H1 in 1920 with the same forcing but slightly altered initial atmospheric conditions and integrated to 2100.

There are three-dimensional ocean velocity, temperature and salinity as well as sea surface wind stress in the model output. However, sea surface height is accessible only in CESM-H1 but not CESM-H2 or CESM-H3. Accordingly, a decomposition of upwelling transport into components associated with horizontal mass-flux divergence caused by geostrophic and ageostrophic flows can be made only for CESM-H1.

Upwelling transport

The upwelling transport (UT) is computed as the horizontal integration of model-simulated vertical velocity zonally within 20 model grids (~200 km) from the coast:

$$\text{UT}(z, t) = \int \int w(x, y, z, t)\, \mathrm{d}x \mathrm{d}y \tag{1}$$

where w is the vertical velocity and $x, y, z,$ and t are the zonal, meridional, vertical, and temporal coordinates, respectively. The northern and southern boundaries for integration are 48° N and 23° N for CalCS, 15° S and 45° S for HCS, 36° N and 15° N for CanCS, and 10° S and 30° S for BCS, respectively. Similarly, the coastal upwelling transport is defined as the horizontal integration zonally within five model grids (~50 km) from the coast. The (coastal) UTI is defined as the value of (coastal) upwelling transport at its peaking depth, that is, 30 (20) m for CalCS, 40 (40) m for HCS, 40 (30) m for CanCS and 40 (30) m for BCS. As to the upwelling in CMIP6 CGCMs, we first bilinearly interpolate w in the individual CMIP6 CGCMs onto the grids of POP2 of CESM-H. Then UTI is computed according to equation (1) on the basis of the ensemble mean w.

The upwelling transport can be further decomposed into components associated with horizontal mass-flux divergence caused by geostrophic and ageostrophic flows, respectively. Under the rigid lid approximation for the sea surface, the geostrophic upwelling transport (UT$_g$) is computed as[17]:

$$\text{UT}_\text{g}(z, t) = \int \int \int_z^0 \left(\frac{\partial u_\text{g}(x, y, s, t)}{\partial x} + \frac{\partial v_\text{g}(x, y, s, t)}{\partial y} \right) \mathrm{d}s \mathrm{d}x \mathrm{d}y \tag{2}$$

where s is the dummy variable in integral and $\mathbf{u}_\text{g} = (u_\text{g}, v_\text{g})$ is defined as $\left(-\frac{1}{f\rho_0} \frac{\partial p}{\partial y}, \frac{1}{f\rho_0} \frac{\partial p}{\partial x} \right)$ with f the Coriolis parameter varying with latitude, ρ_0 the reference seawater density and p the seawater pressure, except along the coastal boundary where $\mathbf{u}_\text{g}$ is set as zero. The value of p is calculated on the basis of the hydrostatic approximation; that is,

$p = \rho_0 g \eta + \int_z^0 \rho(x, y, s, t)\, g \mathrm{d}s$, with η the sea surface height, g the gravity acceleration and ρ the in situ seawater density. The horizontal divergence of $\mathbf{u}_\text{g}$ is computed following the discretization scheme in POP2. Once UT$_g$ is obtained, the ageostrophic upwelling transport UT$_a$ is computed by subtracting UT$_g$ from UT.

WUI

The WUI is defined as the total Ekman transport into/out of the integration region as[19,20]:

$$\text{WUI}(t) = \int \int \frac{\partial U_E(x, y, t)}{\partial x} + \frac{\partial V_E(x, y, t)}{\partial y} \mathrm{d}x \mathrm{d}y \tag{3}$$

where $\mathbf{U}_E = (U_E, V_E)$ is defined as $\frac{\tau}{\rho_0 f} \times \mathbf{k}$ with $\tau = (\tau_x, \tau_y)$ the surface wind stress and $\mathbf{k}$ the unit vector pointing upwards, except along the coastal boundary where $\mathbf{U}_E$ is set as zero. The horizontal divergence of $\mathbf{U}_E$ is computed using the same discretization scheme as that of $\mathbf{u}_\text{g}$. Note that equation (3) accounts for the vertical velocity at the surface Ekman layer base via the coastal divergence/convergence due to the cross-shore Ekman transport driven by the alongshore wind stress and via the Ekman pumping driven by the wind stress curl $\partial \tau_y / \partial x - \partial \tau_x / \partial y$ (refs. [19,20]). As to the WUI in CMIP6 CGCMs, we first bilinearly interpolate τ in the individual CMIP6 CGCMs onto the grids of POP2. Then WUI is computed according to equation (3) on the basis of the ensemble mean τ.

Data availability

The CESM data used in this work are available from http://ihesp.qnlm.ac and https://ihesp.github.io/archive/products/ds_archive/Sunway_Runs.html. The CMIP6 model data can be downloaded from https://esgf-node.llnl.gov/search/cmip6/. The multi-scale ultra-high-resolution SST data are provided by NASA from their website (https://archive.podaac.earthdata.nasa.gov/podaac-ops-cumulus-protected/MUR-JPL-L4-GLOB-v4.1). The fishing effort data are provided by Global Fishing Watch (https://globalfishingwatch.org/dataset-and-code-fishing-effort/). The chlorophyll-a concentration data are obtained from https://oceandata.sci.gsfc.nasa.gov.

Code availability

The CESM-H code used in this work is available via ZENODO: https://doi.org/10.5281/zenodo.3637771 (ref. [44]). The MatlabR2016b is used for plotting.

References

42. Chang, P. et al. An unprecedented set of high-resolution Earth system simulations for understanding multiscale interactions in climate variability and change. *J. Adv. Modeling Earth Syst.* **12**, e2020MS002298 (2020).

43. Taylor, K. E., Stouffer, R. J. & Meehl, G. A. An overview of CMIP5 and the experiment design. *Bull. Am. Meteorol. Soc.* **93**, 485–498 (2012).

44. Wan, W. lgan/cesm_sw_1.0.1: some efforts on refactoring and optimizing the Community Earth System Model (CESM1.3.1) on the Sunway TaihuLight supercomputer (cesm_sw_1.0.1). *Zenodo* https://doi.org/10.5281/zenodo.3637771 (2020).

Acknowledgements

Laboratory. The CESM-H was completed through the International Laboratory for High Resolution Earth System Prediction, a collaboration by the Laoshan Laboratory, Texas A&M University and the National Center for Atmospheric Research.

Author contributions

Competing interests

The authors declare no competing interests.

Additional information

Extended data is available for this paper at https://doi.org/10.1038/s41558-022-01588-y.

Supplementary information The online version contains supplementary material available at https://doi.org/10.1038/s41558-022-01588-y.

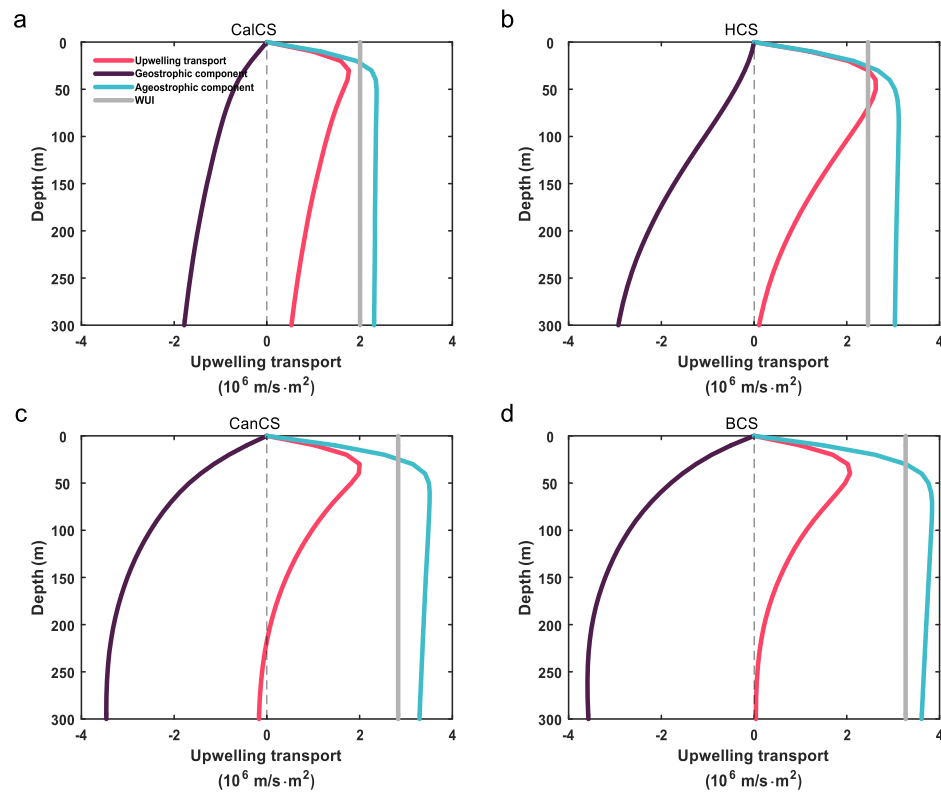**Correspondence and requests for materials** should be addressed to Lixin Wu.

Peer review information *Nature Climate Change* thanks David Rivas and the other, anonymous, reviewer(s) for their contribution to the peer review of this work.

Reprints and permissions information is available at www.nature.com/reprints.
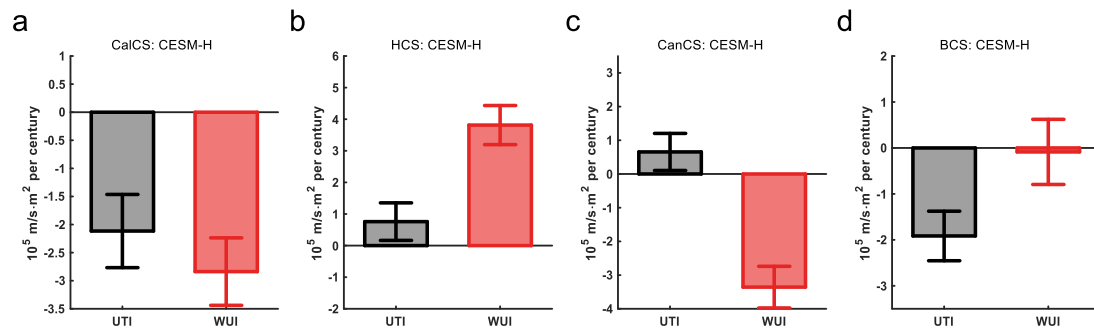
Extended Data Fig. 1 | Simulated 2003–2021 annual mean SST bias in the CESM-H and CMIP6 CGCM ensemble means. The bias is with respect to the observed SST from the Multi-scale Ultra-high Resolution (MUR) SST dataset for the CESM-H ensemble mean (**a**–**d**) and CMIP6 CGCM ensemble mean (**e**–**h**) in the CalCS (**a**,**e**), HCS (**b**,**f**), CanCS (**c**,**g**) and BCS (**d**,**h**). A spatial mean SST bias over the shown region is subtracted from each panel to highlight the SST bias related to the upwelling dynamics.
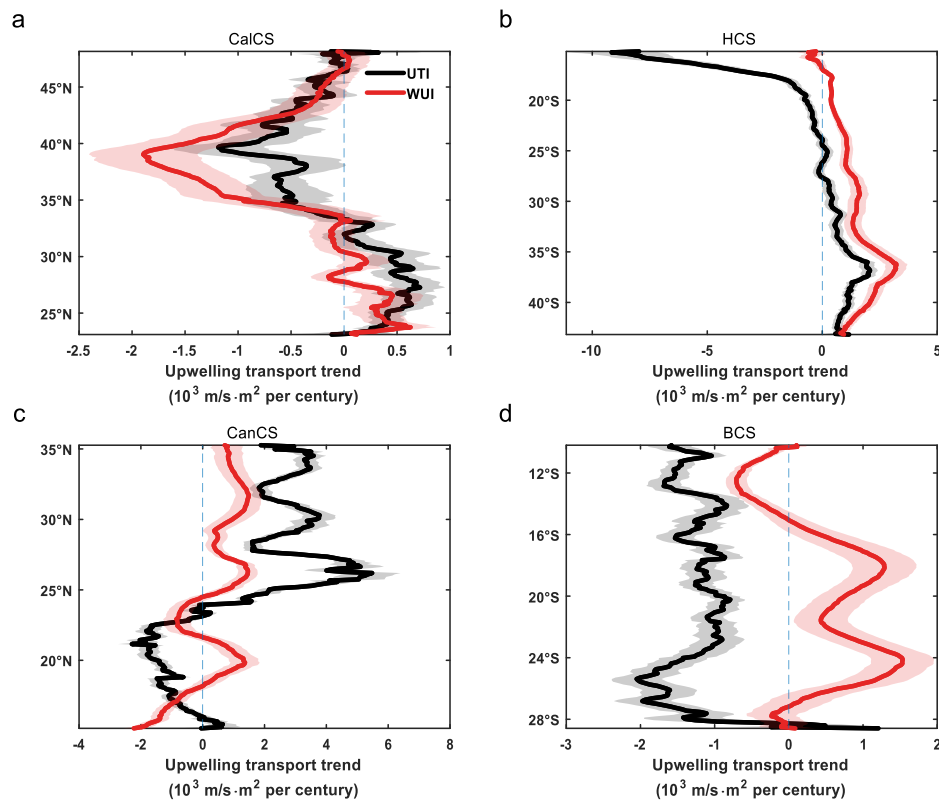
Extended Data Fig. 2 | Effects of geostrophic flows on the climatological mean upwelling transport in the EBUSs. The 1920–2005 annual mean upwelling transport (red) and its decomposition into components caused by horizontal mass flux divergence of geostrophic (purple) and ageostrophic (blue) flows for one member of CESM-H ensemble in the (**a**) CalCS, (**b**) HCS, (**c**) CanCS and (**d**) BCS. The grey line denotes the climatological mean WUI.
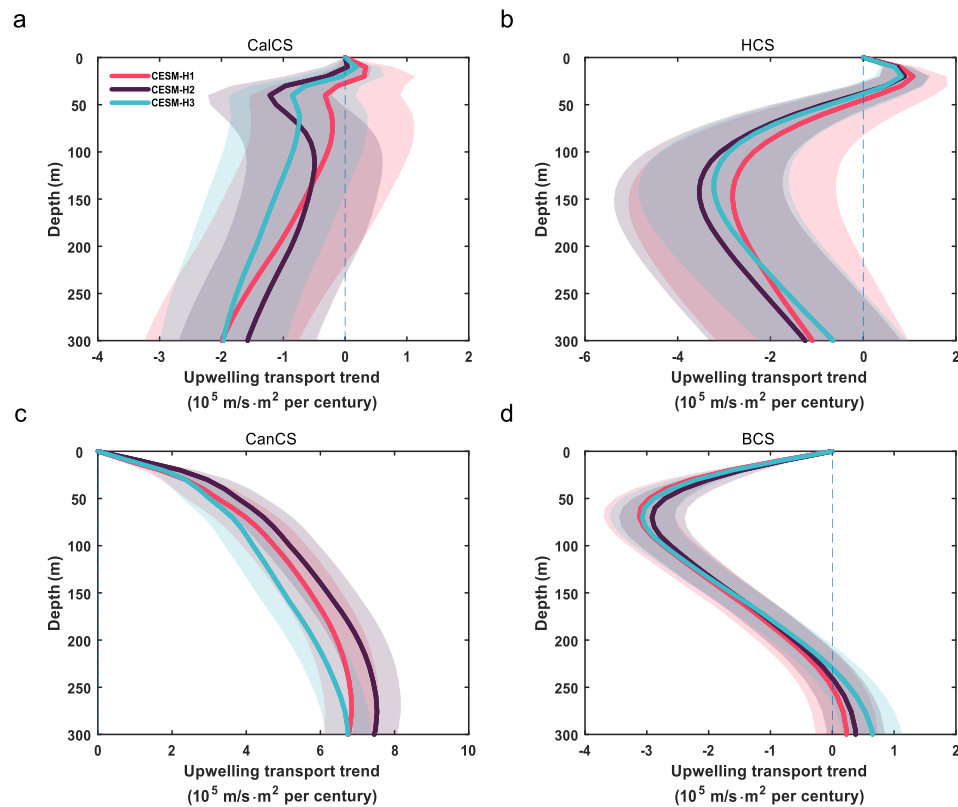
Extended Data Fig. 3 | Relationship between the long-term changes of warm-season mean upwelling transport intensity (UTI) and WUI in the EBUSs under greenhouse warming. The slope of the linear trend of warm-season mean UTI and WUI during 2006–2100 for the CESM-H ensemble mean in the (**a**) CalCS, (**b**) HCS, (**c**) CanCS, and (**d**) BCS, respectively. The errorbar denotes the 90% confidence interval for the slope. The warm season is defined as May-August and November-February in the northern and southern hemispheres, respectively. The sample size, that is, the number of time records used to derive the confidence interval is 95.
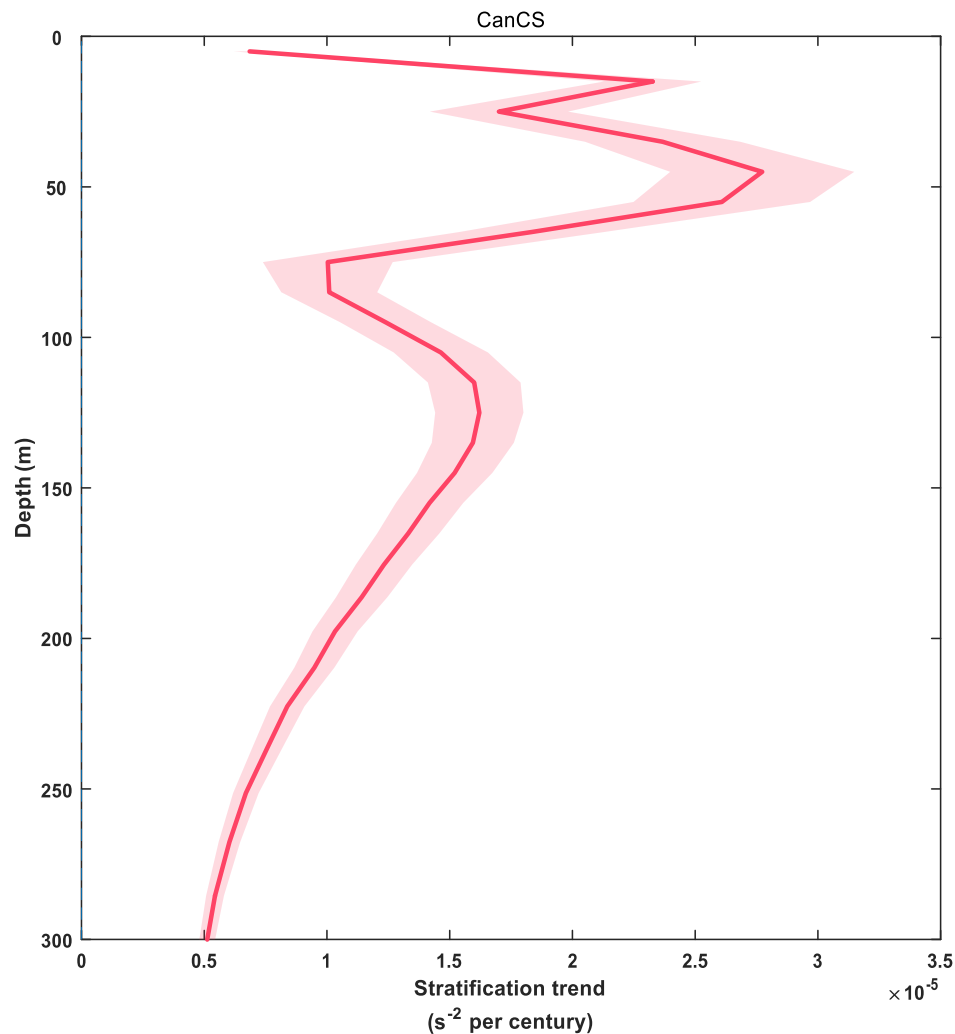
Extended Data Fig. 4 | Relationship between the long-term changes of annual mean upwelling transport intensity (UTI) and WUI in the EBUSs under greenhouse warming at different latitudes. The slope of the linear trend of annual mean UTI and WUI during 2006–2100 in the individual ~0.1° latitudinal bands for the CESM-H ensemble mean in the (**a**) CalCS, (**b**) HCS, (**c**) CanCS and (**d**) BCS, respectively. The shading denotes the 90% confidence interval for the slope. The sample size, that is, the number of time records used to derive the confidence interval is 95.

Extended Data Fig. 5 | Long-term changes of annual mean upwelling transport in the EBUSs under greenhouse warming for individual CESM-H members. The slope of linear trend of annual mean upwelling transport during 2006–2100 for the individual CESM-H members in the (**a**) CalCS, (**b**) HCS, (**c**) CanCS and (**d**) BCS, respectively. The shading denotes the 90% confidence interval for the slope. The sample size, that is, the number of time records used to derive the confidence interval is 95.

Extended Data Fig. 6 | Long-term change of stratification in the CanCS. The slope of linear trend of annual mean squared buoyancy frequency during 2006–2100 for the CESM-H ensemble mean in the CanCS. The shading denotes the 90% confidence interval for the slope. The sample size, that is, the number of time records used to derive the confidence interval is 95.

Extended Data Table. 1 | A list of CGCMs in CMIP6 used in this study

CMIP6	Oceanic Resolution	Scenario	CMIP6	Oceanic Resolution	Scenario
1.CAMS-CSM1-0	1°	Hist, SSP5-8.5	**13.FIO-ESM-2-0**	1°	Hist, SSP5-8.5
2.CESM2-WACCM	1°	Hist, SSP5-8.5	**14.GISS-E2-1-G**	1°	Hist, SSP5-8.5
3.CESM2	1°	Hist, SSP5-8.5	**15.HadGEM3-GC31-LL**	1°	Hist, SSP5-8.5
4.CIESM	0.5°	Hist, SSP5-8.5	**16.HadGEM3-GC31-MM**	0.25°	Hist, SSP5-8.5
5.CNRM-CM6-1-HR	0.25°	Hist, SSP5-8.5	**17.IPSL-CM6A-LR**	1°	Hist, SSP5-8.5
6.CMCC-ESM2	1°	Hist, SSP5-8.5	**18.MIROC-ES2L**	1°	Hist, SSP5-8.5
7.CNRM-CM6-1	1°	Hist, SSP5-8.5	**19.MIROC6**	1°	Hist, SSP5-8.5
8.CNRM-ESM2-1	1°	Hist, SSP5-8.5	**20.MPI-ESM1-2-HR**	0.5°	Hist, SSP5-8.5
9.CanESM5-CanOE	1°	Hist, SSP5-8.5	**21.MPI-ESM1-2-LR**	2.5°	Hist, SSP5-8.5
10.E3SM-1-1	0.5°	Hist, SSP5-8.5	**22.MRI-ESM2-0**	1°	Hist, SSP5-8.5
11.CanESM5	1°	Hist, SSP5-8.5	**23.NESM3**	1°	Hist, SSP5-8.5
12.EC-Earth3-Veg-LR	1°	Hist, SSP5-8.5	**24.UKESM1-0-LL**	1°	Hist, SSP5-8.5

The model selection is based on the output availability of surface wind stress and vertical velocity. The analysis period combines 1850–2014 from the historical simulations and 2015–2100 from the SSP5-8.5 simulations.